sustainability

Article

Characteristics of Droplet Behaviors during Spray Breakup Process

Feixiang Chang [1], Hongliang Luo [2,*], Panpan Dong [3], Keiya Nishida [4], Yoichi Ogata [4], Ryosuke Hara [5], Kenji Uchida [5] and Wu Zhang [5]

[1] School of Mechanical Engineering, Jiangsu University of Science and Technology, Zhenjiang 212100, China
[2] College of Power and Energy Engineering, Harbin Engineering University, Harbin 150001, China
[3] Hebei Jiaotong Vocational and Technical College, Shijiazhuang 050035, China
[4] Graduate School of Advanced Science and Engineering, Hiroshima University, 1-4-1 Kagamiyama, Higashi-Hiroshima 739-8527, Japan
[5] Mazda Motor Corporation, 3-1 Shinchi, Fuchu-cho, Aki-gun, Hiroshima 730-8670, Japan
* Correspondence: luohl@hrbeu.edu.cn

Abstract: The variation of droplet parameters during the spray breakup process affects the droplet deposition behavior and accurate application. The aim of this study was to experimentally investigate droplet behaviors along the penetration direction with respect to spray propagation. Particle image analysis (PIA) was applied to obtain the characteristics of droplets at three representative stages (namely, initial, quasi-steady, and end stages) after the start of injection (ASOI). The effects of timing and location on the spray characteristics were thoroughly investigated. First, different morphological changes of spray (droplets, ligaments, and bags) during spray breakup were observed. The experimental results show that droplet size and velocity distinctly increase from upstream to downstream at the initial stage. However, at the quasi-steady and end stages, droplet velocities are similar, and the effects of location are not evident. This indicates that location has a significant effect on droplet behaviors at the initial stage. The mean minimum distance (MD) of droplets first increases considerably and then decreases from upstream to downstream, suggesting that the droplets disperse better at midstream. Moreover, the mean MD at the initial stage exceeds that at the quasi-steady and end stages, denoting that the droplets disperse better with time. Finally, the geometric parameter of droplets and the key stage selection are important for predicting the interaction between the droplets and surfaces.

Keywords: liquid spray; morphologic changes; diameter; velocity; minimum distance

Citation: Chang, F.; Luo, H.; Dong, P.; Nishida, K.; Ogata, Y.; Hara, R.; Uchida, K.; Zhang, W. Characteristics of Droplet Behaviors during Spray Breakup Process. *Sustainability* **2023**, *15*, 9356. https://doi.org/10.3390/su15129356

Academic Editor: Talal Yusaf

Received: 29 March 2023
Revised: 23 May 2023
Accepted: 7 June 2023
Published: 9 June 2023

1. Introduction

The main goals of developing direct-injection spark-ignition (DISI) engines are reducing pollutant emissions and improving combustion efficiency to cope with severe global crises, including environmental risk and energy resource restrictions [1]. A key factor in achieving this goal is the air–fuel mixture quality, which is significantly affected by the microscopic characteristics of sprays. The interaction between the spray and the air has to be thoroughly understood.

To investigate the spray atomization process, comprehensive experiments were conducted to obtain the droplet behavior [2]. Droplet diameter, velocity, and number density have been investigated using various advanced laser diagnostic techniques, such as particle image velocimetry (PIV), phase Doppler particle analyzer (PDPA), and PIA. Urban et al. [3] simultaneously calculated the drop size as well as the axial and radial velocity components of a spray using the phase-Doppler technique. They found that peripheral droplets were highly stable, and intense secondary atomization was confined to the spray center. Deshmukh and Ravikrishna [4] investigated the microscopic structures of diesel sprays under atmospheric and high gas pressures. The results showed that the ligaments tended to become smaller and spread radially with increasing injection pressure. Moreover, atomization was significantly improved under high gas-density conditions. Kashdan et al. [5] quantitatively measured non-spherical objects using a digital image analysis technique. They also compared the phase-Doppler anemometry (PDA) data and particle/droplet image analysis (PDIA) spray data and found excellent agreement among the measured diameters in the range 10–90 μm. Blaisot and Yon [6] proposed a new approach for spray sizing based on the modeling of image formation and qualified drop shapes using four morphological parameters. Moreover, spherical and elliptical droplets were also compared with the droplets formed by other techniques. Komada et al. [7] investigated the size and velocity of droplets under an injection pressure of 80 MPa using laser-2-focus (L2F) velocimetry. They found that the droplet velocity decreased from the center toward the spray periphery. Shadowgraphy and PIV methods were used by Goldsworthy et al. [8] to determine the effect of various fuel viscosities on the droplet velocity and size of a diesel spray in a high-pressure chamber. They found that larger droplets were formed because of the high fuel viscosity. Pathania et al. [9] studied the droplet size statistics along the spray penetration axis using the PDPA technique. The average droplet diameter was approximately 100 μm and increased along the axial distance below the nozzle tip. The results further showed that the average droplet size did not vary significantly with time ASOI. Jing et al. [10] used the PDPA approach to evaluate the time-averaged Sauter mean diameter (SMD) and velocity as functions of the spatial location of the sprays of diesel, gasoline, and their mixture. They discovered that the SMD and droplet velocity decreased as the axial distance from the nozzle increased. Wang et al. [11] studied the microscopic and macroscopic characteristics of diesel spray with split injection using the PDPA technique. The findings showed that strong collisions (both primary and secondary) resulted in larger droplets for split injection than for single injection. Moreover, the second spray plume penetrated quicker than the first one, and the difference of the tip velocity was as high as 10 m/s. Many studies have focused on the droplet breakup model using dimensionless numbers, such as the Weber number (*We*). Several researchers [12,13] have shown image sequences of the fragmentation process for a wide range of parameters. Moreover, they have summarized the breakup modes (categorized as vibrational, bag, shear or stripping, and catastrophic) and transitional breakup modes. The critical or transition *We* is an approximate value. The reported values vary among different studies. However, because the liquid spray is a cluster of fuel droplets undergoing complex interactions, the single-droplet phenomenon fails to represent the spray breakup process. Therefore, the spray breakup process requires further investigation.

The spray evolution has been thoroughly investigated by many researchers. Feng et al. [14] selected one capture location at the periphery and investigated the droplet behavior in the transient spray using the PDIA method ASOI. The results indicate that discrete droplets and their sizes can be characterized into three distinct phases: latent (0–0.5 ms), injection (0.5–2.1 ms), and free stages (after 2.1 ms). In addition, the diameters of droplets were in the range of 7.0–46.5 μm. Lebedevas et al. [15] obtained the liquid jet breakup characteristics of microalgae oil (MAO100) at elevated temperatures using laser diffraction. The SMD distribution differed within the temporal evolution of the fuel spray for the injection, half-time, and end-time stages of jet propagation. They also found that the preheated microalgae oil was dominant in the following droplet sizes: $d \leq 40–50$ μm (~20%) and $d \leq 120$ μm (~50%). Luo et al. [16] investigated the near-nozzle spray characteristics at the initial and end stages using a high-resolution camera. They found that the spray structures could be classified as mushroom, steeple, and cylindrical shapes at the initial stage. At the end stage, droplets are responsible for injector deposition. Bae and Kang [17] gained physical insight into the development of a transient diesel spray using a charge-coupled device (CCD) camera. They found that ligaments were generated from the disturbed spray surfaces as the spray velocity increased. Then, at the early stages of injection, the ligaments broke up into droplets. Payri et al. [18] applied the PIV technique to measure the velocity field of a diesel spray. However, their observations were restricted to the steady state of a fully developed spray. Liu and Duan et al. [19] identified the bubble, transition, and annular flows in an effervescent atomizer by high-speed digital images. They found that the droplet generation process at various air-to-liquid ratios (ALR) resulted in spray unsteadiness, and all droplet size groups displayed spray unsteadiness. Crua et al. [20] investigated the initial stage of diesel spray formation and primary breakup using high-speed video cameras. They observed ripples around a stagnation point on the surface of the cap under non-evaporation conditions, which might have been generated by shearing instabilities at the liquid–gas interface. Pei et al. [21] studied characteristics of free and impingement sprays fueled with different fuels by the PDA system. The results showed that a large fraction of the incident droplets adhered to the wall. The diameters of the reflected droplets were reduced compared to those of the incident droplets.

To have a deeper understanding of the spray dynamics, Wang et al. [22] investigated the shock-induced breakup of two identically sized water droplets in tandem formation. They discovered that the We varies between 13 and 180 and that the distance between the droplets varies between 1.2 and 10.5 times the droplet diameter. The formation of smaller bags in bag and bag-and-stamen morphologies reflected the attenuation of the breakup intensity. Zhao et al. [23] investigated two neighboring droplets at We = 12.3 in the bag-breakup regime with the normalized separation distance S less than 3, and they found a coalescence mode at $S < 1.3$ and a puncture mode at the higher S of the two tandem droplets. Chen et al. [24] discovered the effect of ambient temperature and injection pressure on the spray atomization of diesel and diesel–polyoxymethylene dimethyl ether ($PODE_{3\text{-}4}$) at 20 and 50% fractions of the volume. The results showed that with the increase of temperature and injection pressure, the droplet size and SMD of diesel and diesel–$PODE_{3\text{-}4}$ decreased. Moreover, the droplet size of diesel fuel is larger than that of dual fuel blends. Khaleghi et al. [25] investigated the influence of turbulence on secondary droplet disintegration. The turbulent intensity has great influence on the critical We value. The effect of turbulence is much less when the ambient pressure is very high. Amedorme [26] studied the variation of droplets injected by a swirl atomizer at different locations. The SMD increased along the center line in the axial direction. However, when the injection pressure increased, the value of the SMD decreased. The nozzle with the smaller exit-orifice diameter out of the two compared had a smaller SMD. Chang et al. [27] adopted a spray slicer to cut the dense spray into thin flakes with the objective of observing discrete droplets. They found droplets with high V_y are more likely to fly away from the impinging wall. Moreover, droplets with diameters larger than 20 μm increase at the downstream due to the breakup of ligaments.

From the foregoing discussions, the PDPA, PDA, PIV, and L2F diagnostic techniques can be applied to detect the droplet behavior in the dense spray region. However, these methods fail to obtain droplet images, so PIA may be implemented as a solution. However, the capture of clear droplet images in the dense regions of the spray is impossible owing to the high number density of droplets, mainly occurring in the periphery of spray plumes [28]. For accurate droplet recognition, the focus must be on the dilute spray region where the density of the liquid phase is suitable for imaging. The microscopic imaging of sprays has proven to be a highly useful tool for evaluating the primary breakup and detecting the behavior of droplets [5]. In order to figure out the spray breakup process, droplet behaviors at different stages need to be observed and compared.

From the previous studies on the microscopic characteristics of sprays, three distinct stages (initial, quasi-steady, and end stages) of spray were observed during spray evolution. Although a quasi-steady spray was thoroughly investigated using the PIA method, the microscopic characteristics of spray need to be thoroughly understood at the initial and end stages. In particular, the droplet distribution from upstream to downstream at different stages needs to be investigated and compared. Related reports on using PIA to investigate the spatial distribution of droplets propagating at the periphery have seldom been reported. As the spray evolves, the droplet size and velocity evidently change, and the interaction between droplets and ambient gas becomes extremely complex. Accordingly, the aim of this study was to characterize the droplet behavior at the spray periphery at the three distinct stages. Experiments were performed in a constant volume chamber (CVC) using the PIA technique. First, morphological changes at the spray periphery were captured. Then, the effects of timing and location on the transient changes in the droplet velocity and diameter were examined and compared. Finally, the *We* and MD among the droplets are discussed.

2. Experimental System and Conditions

2.1. Experimental Setup

A schematic of the PIA system used to investigate the microscopic spray characteristics is shown in Figure 1. The experimental setup (Figure 1) for the microscopic spray analysis consisted of a fuel injection system, a CVC with an air purging system, and an optical system. An Nd: YAG laser with a 532 nm wavelength was employed to provide homogenous illumination in the chamber. The interval between the two laser pulses was 6 ns. A diffuser with a diameter of 100 mm was used to expand the light beam. A CCD camera (Flowtech Research Inc., FtrNPC, Yokohama City, Japan) combined with three teleconverters (number: 3; model: Kenko Tokina, N-AF TELEPLUS MC4; magnification: $1.4 \times 1.4 \times 2$) was used to capture microscopic images. The optical techniques used are listed in Table 1. The time interval between two frames was 0.8 μs, and the frame size was 1600×1200 pixels. The resolution of droplet images was 1.31 μm/pixel. The laser beam was collinear with the camera axis, providing high illumination intensity and uniform illumination. This enabled the capture of high-quality images. A synchronizing signal generator (VSD 2000) was utilized to control the triggering pulses of the laser, injection, and CCD camera. The experiments in this study were conducted under ambient pressure conditions in a CVC. A CVC experimental setup was designed to understand the behavior of fuel sprays in cold, non-reacting environment. In the optical system, the CVC consisted of four flanges with quartz windows. A six-hole injector injected toluene as the test fuel, the physical properties of toluene are similar to that of gasoline fuel. The target hole diameter was 0.166 mm. A schematic of the injector and spray plumes is shown in Figure 2. The set injection pressure was 20 MPa, and the injection duration was 3.2 ms. The experimental conditions are listed in Table 2.

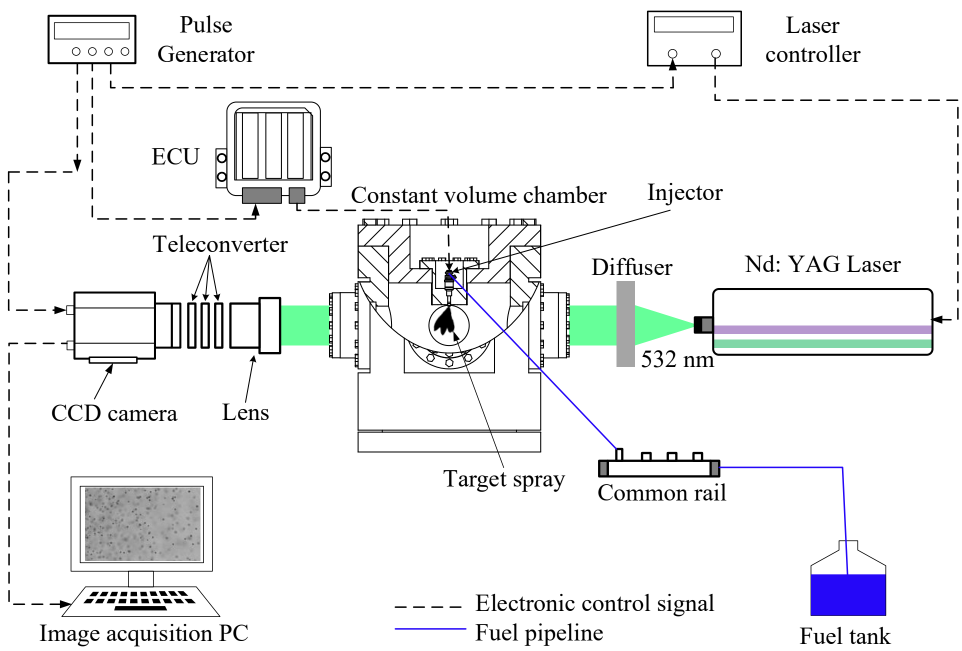

Figure 1. Experimental setup.

Table 1. Optical system.

Camera Type	CCD Camera
Teleconverter Model	Kenko Tokina, N-AF TELEPLUS MC4
Teleconverter Magnification	1.4 × 2, 2.0 × 1
Laser Type	Nd: YAG
Wavelength	532 nm
Interval Time	0.8 µs
Frame Size	1600 × 1200 pixels

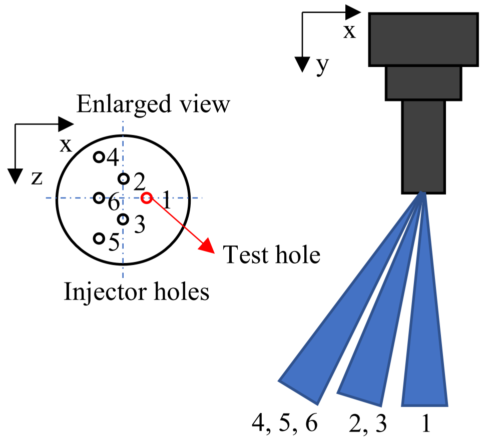

Figure 2. Schematic of injector and spray plumes.

Table 2. Experimental conditions.

Injector	
Hole Geometry	Straight hole
Hole Number	6
Nozzle Hole Diameter (*d*)	0.16 mm
Length to Diameter (*L/D*)	2
Injection Condition	
Fuel	Toluene
Injection Pressure (P_{inj})	20 MPa
Injection Duration	3.2 ms
Ambient Condition	
Ambient Gas	Nitrogen
Ambient Pressure (P_{amb})	0.1 MPa
Ambient Temperature (T_{amb})	298 K

Capture locations for the different stages are depicted in Figure 3. The injector tip was set as the initial point (0, 0), and three typical timings were set at 1.0, 2.0, and 3.3 ms ASOI. The arrow to the right is the positive direction of the X axis, and the down arrow represents the positive direction of the Y axis. The sprays at the three timings represent the initial, quasi-steady, and end stages of spray development. In this work, three capture locations were identified: upstream (30 mm), midstream (50 mm), and downstream (70 mm). At each timing, the three selected capture locations can describe the development of spray from upstream to downstream. Locations (5.5, 30), (8, 50), and (4.5, 70) were selected as acquisition points for droplet characteristics at 1.0 ms ASOI. Positions (5.5, 30), (8, 50), and (8.5, 70) were used to record the distribution of droplets at 2.0 ms ASOI. Locations (3, 30), (7, 50), and (7, 70) were selected to obtain the droplet behavior at 3.3 ms ASOI. The principle of selecting the radial distance of the capture location is elaborated in [29]. The capture timings and locations are summarized in Table 3.

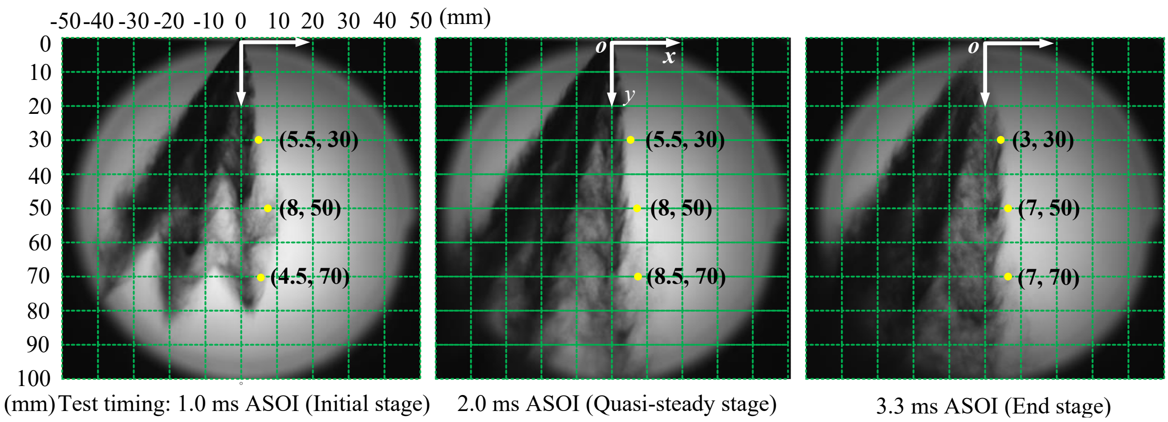

Figure 3. Capture locations at different stages.

Table 3. Capture timings and locations.

Case #1	Timing		1.0 ms ASOI (Initial stage)	
	Locations	(5.5, 30)	(8.0, 50)	(4.5, 70)
Case #2	Timing		2.0 ms ASOI (Quasi-steady stage)	
	Locations	(5.5, 30)	(8.0, 50)	(8.5, 70)
Case #3	Timing		3.3 ms ASOI (End stage)	
	Locations	(3.0, 30)	(7.0, 50)	(7.0, 70)

The volumetric flowrate's variation with time ASOI is depicted in Figure 4. It was measured using the Zeuch technique in which the injection was triggered in a closed, fixed-volume chamber filled with toluene. The pressure level in the measurement chamber was maintained at 2 MPa. The injection pressure was the same as that used in the experiment. Finally, the injection rate curve could be derived. The three typical timings are marked in red in Figure 3. Further details regarding the principle of the Zeuch technique are presented in [30].

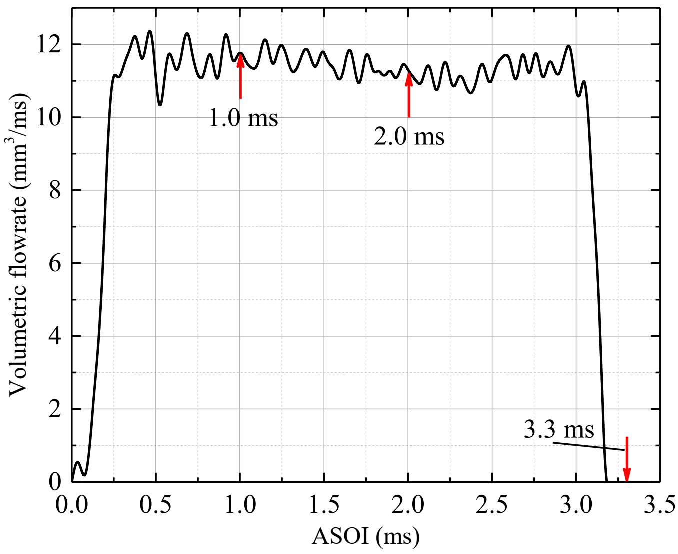

Figure 4. Volumetric flowrate varied with time ASOI.

2.2. Image Processing Method

The image processing method applied to the calculations is presented in Figure 5. The time interval between the two frames was set at 0.8 μs. The measurement principle of the droplet velocity is based on the change in the droplet displacement. The Canny algorithm was applied to extract the shape characteristics of droplets from two sequential frames. These characteristics include roundness, diameter, eccentricity, and other parameters. The roundness of droplets exceeded 0.8, and the droplet diameter was 7–60 μm. The selected spherical droplets shown in Figure 5 are represented by red dots, and the ligaments or non-spherical droplets are represented by white areas. Note that some droplets cannot be simultaneously acquired from the two frames. Finally, the droplet centroid displacement was calculated by matching the corresponding droplets in frames 1 and 2, and the droplet velocity is calculated using the time interval. In Figure 5, the droplet velocity is indicated by colored arrows. Further details pertaining to image processing are presented in [31].

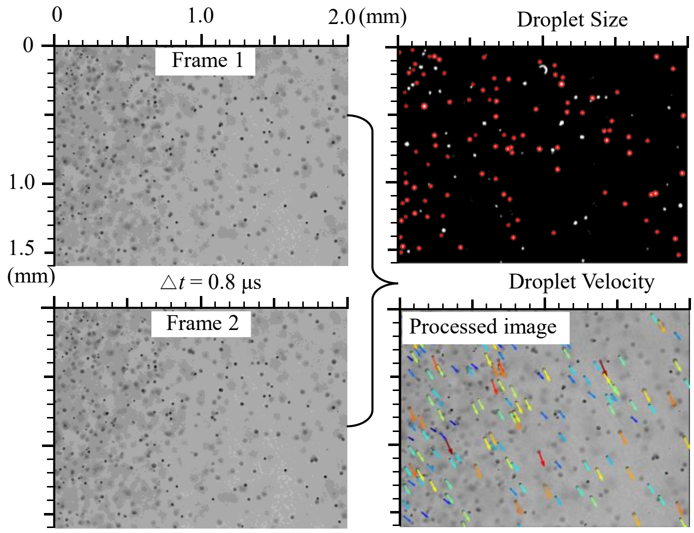

Figure 5. Image processing method.

3. Results and Discussion

3.1. Morphological Changes at Spray Periphery

The spray morphology and MD definition are shown in Figure 6. Two types of information can be obtained from the microscopic images. Non-spherical liquids, such as ligaments and bags, can be observed in Figure 6, and spherical droplets can be calculated by the image processing method presented in Figure 5. Moreover, the MD among droplets is defined in Figure 6. Note that for a particular droplet surrounded by other droplets, the distance between this droplet and each of the surrounding droplets is obtained. Accordingly, several distances are calculated (such as D1, D2, D3, D4, D5, and so on). The MD indicates the degree of the droplet number density at a fixed size window. Details of the mean MD are found in our previous work [31,32].

The morphological changes at the spray periphery are described in Figure 7. In this figure, #1 and #1′ are two successive frames with a time interval of 0.8 μs. The liquid droplet behaviors, such as coalescence and breakup, are depicted in Figure 7a. As shown by #1 in Figure 7a, when two droplets differ in relative velocities, they merge into a single droplet. Furthermore, the two droplets are pinched off from the ends of the ligament, and the remaining ligament contracts to form a third droplet, as shown by #2. The single droplet stretches and eventually breaks up, as shown by #3. This occurs because the rotational kinetic energy exceeds the surface tension energy required to maintain a single mass. Further details regarding the regimes of coalescence and separation are given by the findings of Qian and Law [33]. The morphological changes in the ligament are shown by #4 and #5 in Figure 7b. A strong centrifugal force causes the ligament to elongate. Moreover, due to aerodynamic dragging forces, the bag is drawn out into a form with a thin rim outside and a core drop inside, as shown by #7 and #8 in Figure 7c. For #6, the liquid interior is bright and considered as a bag. However, the bag shape is complicated and considerably varies with time.

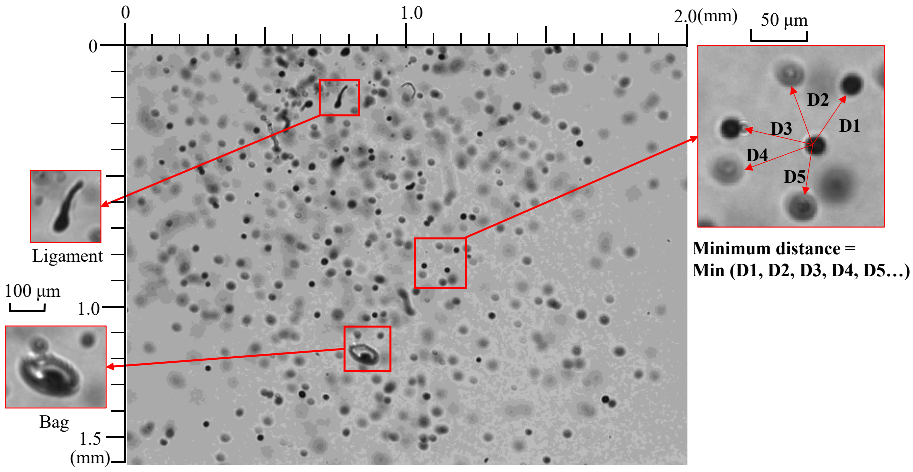

Figure 6. Spray morphology and MD definition.

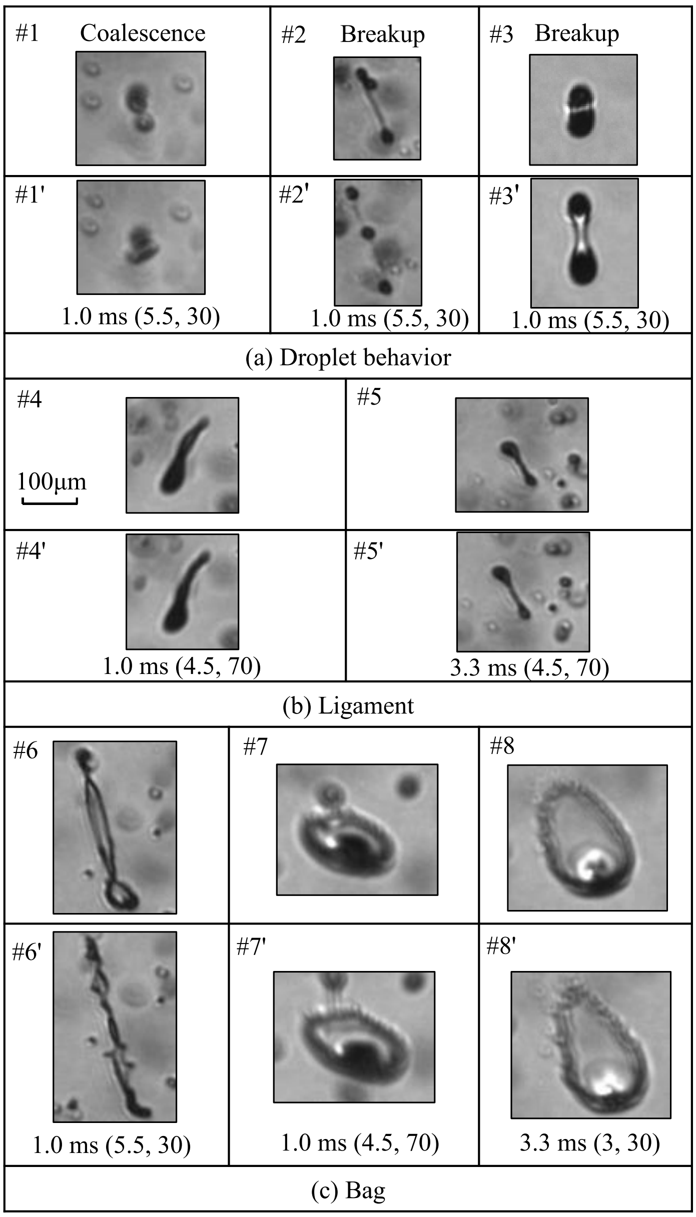

Figure 7. Morphological changes at spray periphery (Δt = 0.8 µs).

The Reynolds number (*Re*)–*We* distribution is depicted in Figure 8. The horizontal and vertical axes represent *Re* and *We*, respectively. Moreover, the numbering shown in this figure corresponds to that in Figure 7. Many of the findings were characterized in terms of a number of non-dimensional categories. In secondary atomization, a drop is deformed by aerodynamic forces, causing it to fragment. The liquid surface tension resists this deformation and tends to restore the spherical shape. Accordingly, *We* (defined as the ratio of aerodynamic forces to surface tension forces) is the most significant parameter for describing the secondary atomization; a larger *We* value denotes greater proclivity toward fragmentation. Another important dimensionless number is *Re*, which is the ratio of aerodynamic forces to ambient viscous forces.

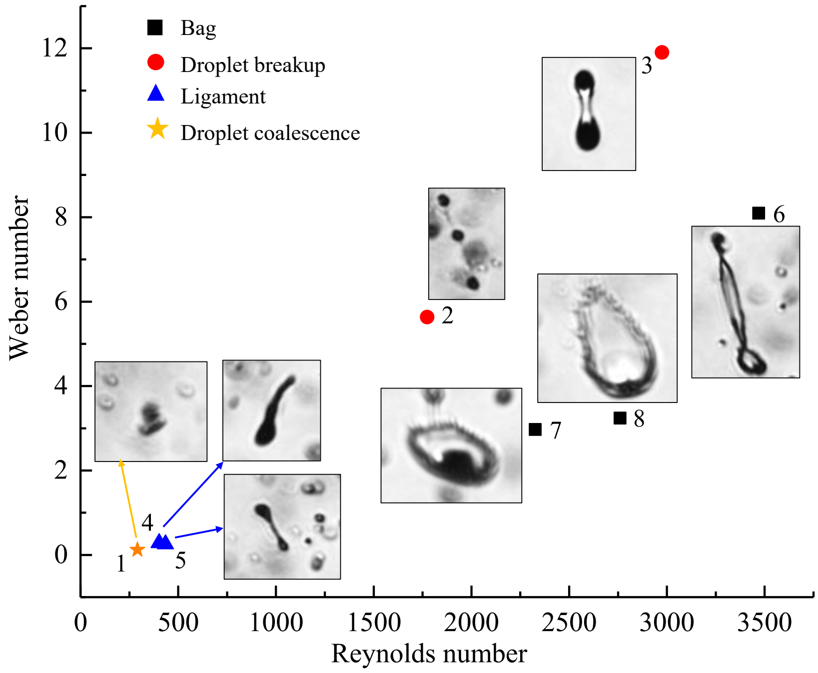

Figure 8. *Re*–*We* distribution.

The equations of *We* and *Re* are as follows:

$$We = \frac{\rho_a {V_D}^2 D}{\sigma_f}, \tag{1}$$

$$Re = \frac{\rho_a V_D D}{\mu_f}, \tag{2}$$

where ρ_a is the ambient gas density; V_D is the relative velocity of the liquid; D is the droplet diameter; σ_f is the surface tension coefficient of fuel; and μ_f is the dynamic viscosity of fuel. To calculate the equivalent area from the droplet images, the boundary of the liquid was selected. Subsequently, the diameter was obtained. The velocity is calculated based on the movement of the liquid centroid. After calculating *We* and *Re*, a map of the *We*–*Re* distribution was drawn. The phenomena of droplet coalescence and shape change of the ligament are in the range of small values of *We* and *Re*. The droplet breakup occurs in the upper region where *We* and *Re* are considerably high. The bag is located in the lower region, and *Re* is similar to that of the droplet breakup. However, the *We* of bag the is much smaller than that of the droplet breakup. In the future, a simple means for establishing these regimes based on the appearance of the liquid droplets will be developed.

3.2. Droplet Diameter–Velocity Distribution

The droplet diameter–velocity distribution is depicted in Figure 9. The effects of timing and location on the droplet behavior are shown in Figure 9a,b. In Figure 9a, the droplet diameter–velocity distributions at upstream appear to be similar. However, at 1.0 ms, the droplet velocity at midstream and downstream considerably exceeds those at 2.0 and 3.3 ms ASOI. As shown in Figure 9b, the droplet velocity increases from upstream to downstream at 1.0 ms ASOI. However, at 2.0 and 3.3 ms ASOI, the droplet velocity distributions are similar from upstream to downstream. These observations indicate that the droplet velocity at 1.0 ms is much greater than those in other cases at downstream. The droplet behavior is elaborated in the next section.

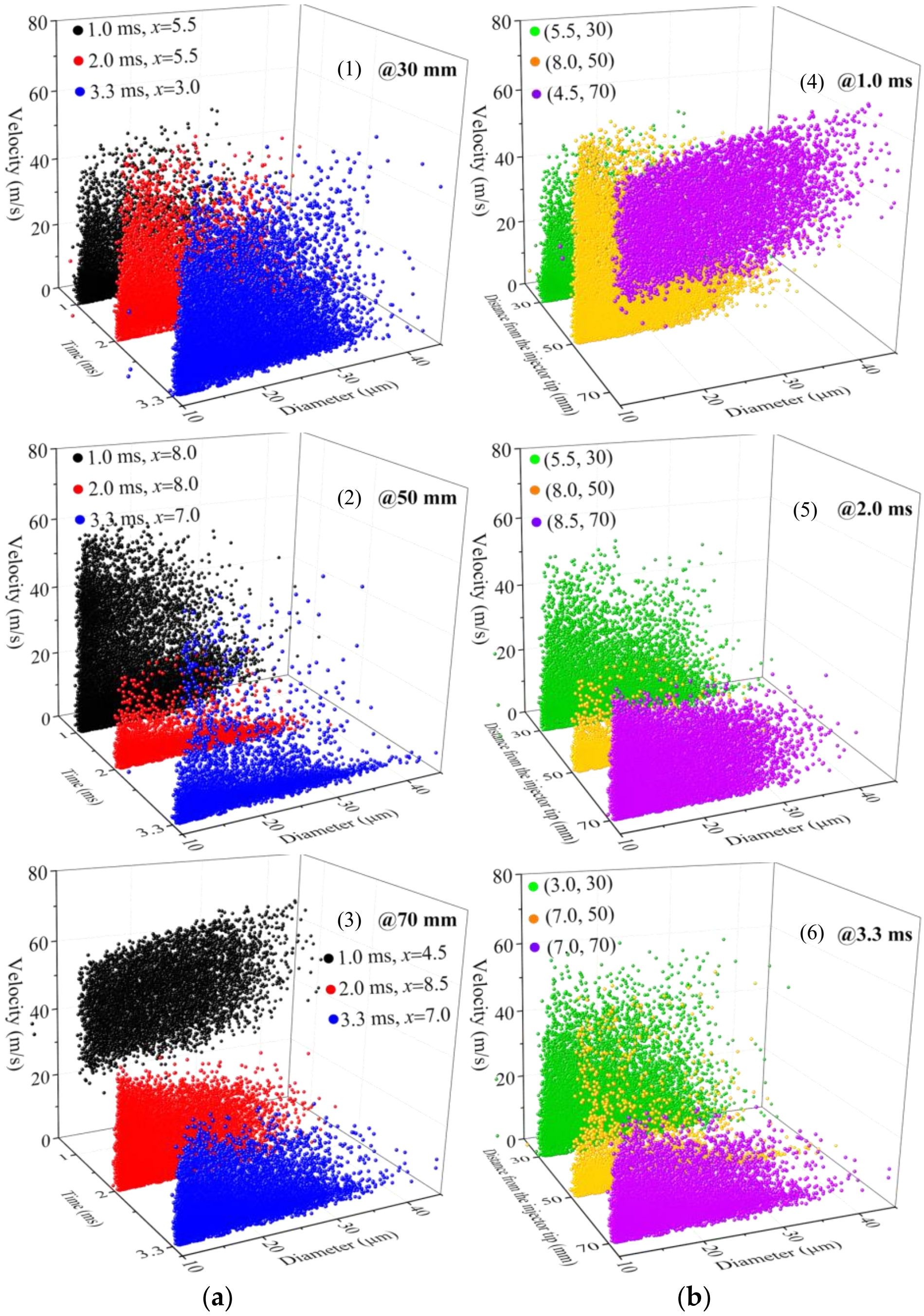

Figure 9. Droplet diameter–velocity distribution. (**a**) Different timings at same location, ((1) 30 mm, (2) 50 mm, and (3) 70 mm); (**b**) different locations at same timing, ((4) 1.0 ms, (5) 2.0 ms, and (6) 3.3 ms).

The droplet velocities in the X and Y directions are compared in Figure 10. In this figure, the specific capture locations are shown by the coordinates on the right. Colored dots represent the droplet velocity under different timings. The velocity along the X axis is V_x (m/s), and that along the Y axis is V_y (m/s). To identify where the droplets are observed, the quadrant numbers are shown on the upper left of Figure 10. The droplet arrow indicates the direction of the droplet's velocity. When droplets are in the first and second quadrants, the droplets move along the direction of spray development. When the droplets are distributed in the third and fourth quadrants, the droplets change their direction of movement due to air entrainment. Because the velocity distribution of droplets is concentrated in the first quadrant, these droplets considerably contribute to the axial and radial expansions of the spray.

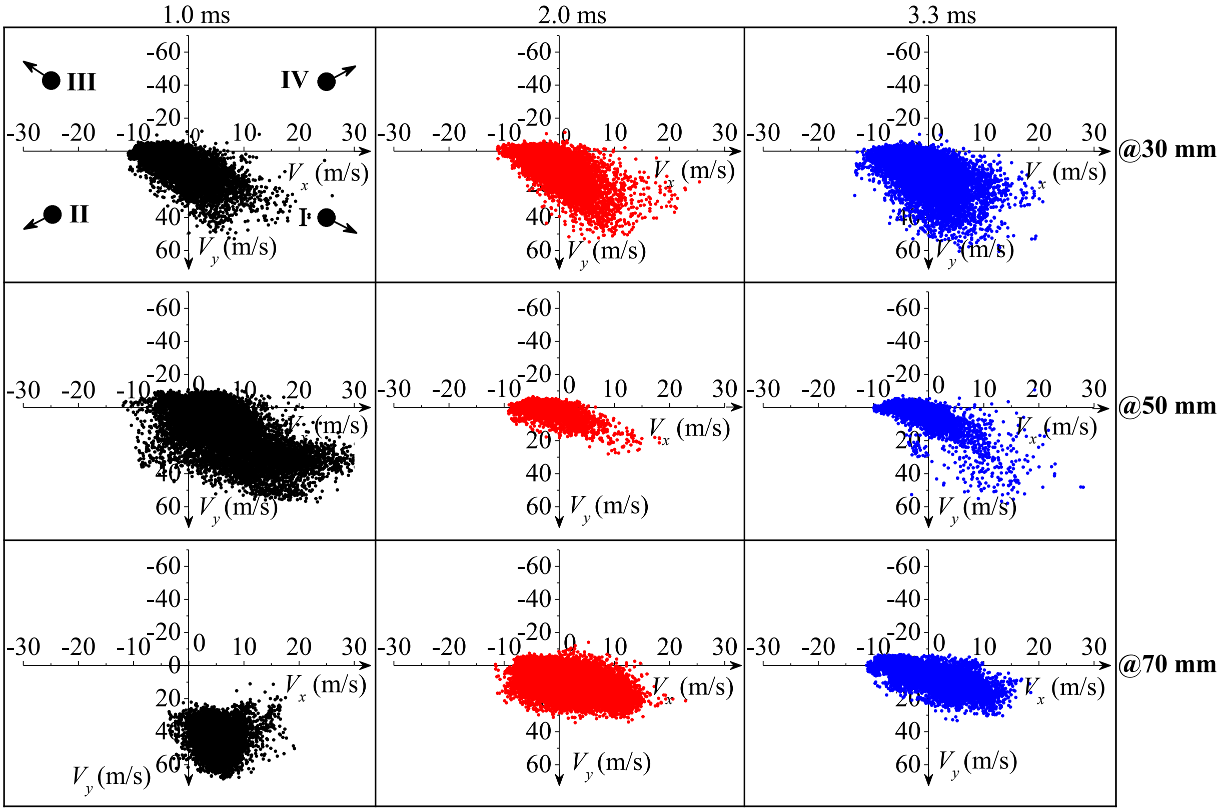

Figure 10. Droplet velocity in the X and Y directions.

To determine the impact of shot timing, note that the droplet velocity distributions are similar at 2.0 and 3.3 ms ASOI from upstream to downstream. However, at midstream, V_x at 1.0 ms greatly increases, contributing to the radial spray expansion. Furthermore, V_y at 1.0 ms ASOI is much higher than that downstream at 2.0 and 3.3 ms ASOI. A possible reason is that the droplets at 1.0 ms are in the initial stage, and those at the periphery perform an important function in the axial and radial expansions of the spray. The droplets at 2.0 and 3.3 ms ASOI are in the quasi-steady and end states, respectively. The results are compared with the studies of Zhou et al. by the PDPA method. Zhou et al. [34] also investigated the macroscopic spray and microscopic droplet diameter, velocity, and temperature through various measurement methods. They found that the spray presented a bowl spray configuration with rapid expansion at the nozzle exit, which is consistent with our work. Due to the air resistance, the droplets at the edge lose most of their kinetic energy and cannot continue to expand. To determine the effect of location, note the similarity of the droplet velocity distributions along the spray development at 2.0 and 3.3 ms (Figure 10). In contrast, the droplet velocity greatly varies from upstream to downstream at 1.0 ms. This occurs because the droplets located at the downstream are near the spray tip, resulting in a high V_y magnitude. Moreover, those located at 50 mm have high V_x magnitudes, contributing to the spray expansion in the radial direction.

The mean velocities of the droplets are shown in Figure 11. The horizontal axis represents the distance from the injector tip, and the vertical axis denotes the mean velocity. Considering the effect of different timings, the mean velocities at 2.0 and 3.3 ms ASOI along the spray development are similar. However, at the midstream and downstream, the mean droplet velocity at 1.0 ms is much larger than those at 2.0 and 3.3 ms ASOI. This occurs because the droplets at 1.0 ms are at the initial stage and play an important role in the axial and radial expansions of the spray. The mean velocity at different locations is depicted in Figure 11b. To determine the effect of different locations, note that for upstream and midstream, the mean velocity at different timings is similar. However, at downstream, the mean droplet velocity at 1.0 ms is much larger than those at 2.0 and 3.3 ms ASOI. This is because at the initial stage, the droplets enable the spray penetration.

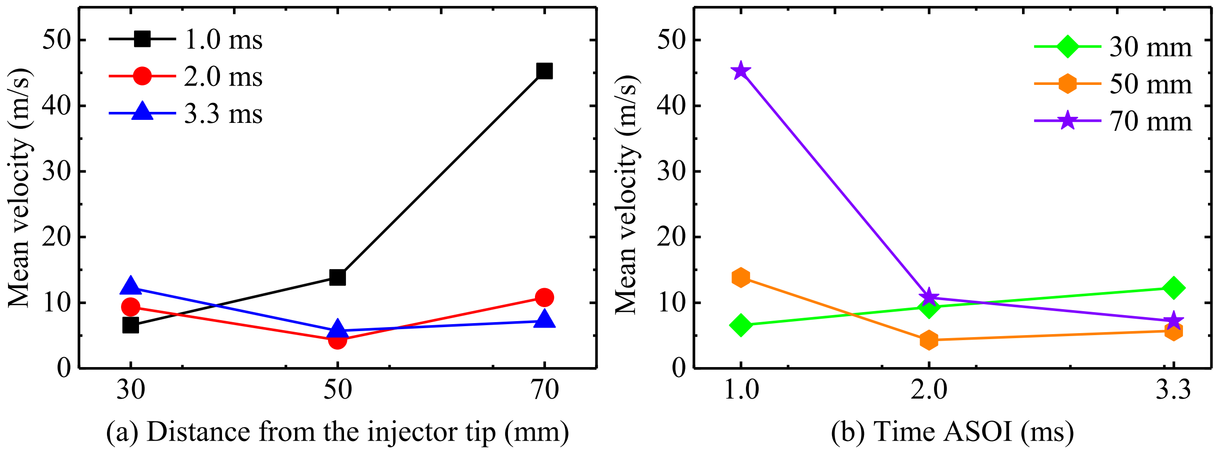

Figure 11. Mean droplet velocity.

3.3. Droplet Size Distribution

The droplet size distribution is shown in Figure 12, where the horizontal and vertical axes represent the droplet diameter and probability, respectively. The solid lines of three different colors shown in Figure 12a represent three different timings. The solid lines of three different colors shown in Figure 12b represent three different locations. To consider the effect of timing on droplet size, note that in Figure 12a, at 30 and 50 mm, the distribution area of the droplet diameter has no distinct differences under different timings. Moreover, the peak droplet diameter is approximately 12 µm. With the spray's development (at 70 mm), the peak decreases from 1.0 to 3.3 ms ASOI, indicating that the droplet diameter increases. A possible reason for this is that the ligaments easily break up into larger droplets owing to aerodynamic resistance. Consequently, numerous larger droplets are generated during spray development. The probability of the droplet diameter ranging from 10 to 16 µm at 1.0 ms is a little lower than that of droplets at downstream at 2.0 and 3.3 ms ASOI. However, when the diameter changes to the larger diameter range (20–45 µm), the droplet diameter probability is the highest at 1.0 ms. Accordingly, the largest SMD also occurs at 1.0 ms. To identify the effect of timing on the droplet size shown in Figure 12b, note that at 1.0 ms, from upstream to downstream, the droplet size increases. This is because the ligaments easily break up into larger droplets owing to aerodynamic resistance. Consequently, numerous larger droplets are generated at downstream. Moreover, at downstream, the capture location was near the spray tip, so the possibility of droplet coalescence increased. This result is consistent with the findings of Lee et al. [35]. However, at 2.0 and 3.3 ms, the droplet size is similar from upstream to downstream. A possible reason is that the sprays at these timings are at the quasi-steady and end states, resulting in satisfactory dispersion at the edge.

The SMD is shown in Figure 13a, and the three colored lines represent different timings. Figure 13a is used to show the effect of different timings on the SMD. At 2.0 and 3.3 ms ASOI, from upstream to downstream, the SMD slightly decreases. However, at 1.0 ms, the SMD noticeably increases. A possible reason is that the spray is at the quasi-steady and end stages at 2.0 and 3.3 ms ASOI, respectively. Droplet dispersion improves from upstream to downstream, and the spray at 1.0 ms is at the initial stage of spray development. In particular, the SMD at downstream is much greater than the SMDs at upstream and midstream. To explain the effect of different locations on the SMD shown in Figure 13b, note that at 2.0 and 3.3 ms ASOI, the SMDs are similar along the direction of spray development. However, the SMD clearly increases from upstream to downstream. This is because the droplets of the spray tip located at downstream are larger and have high velocity.

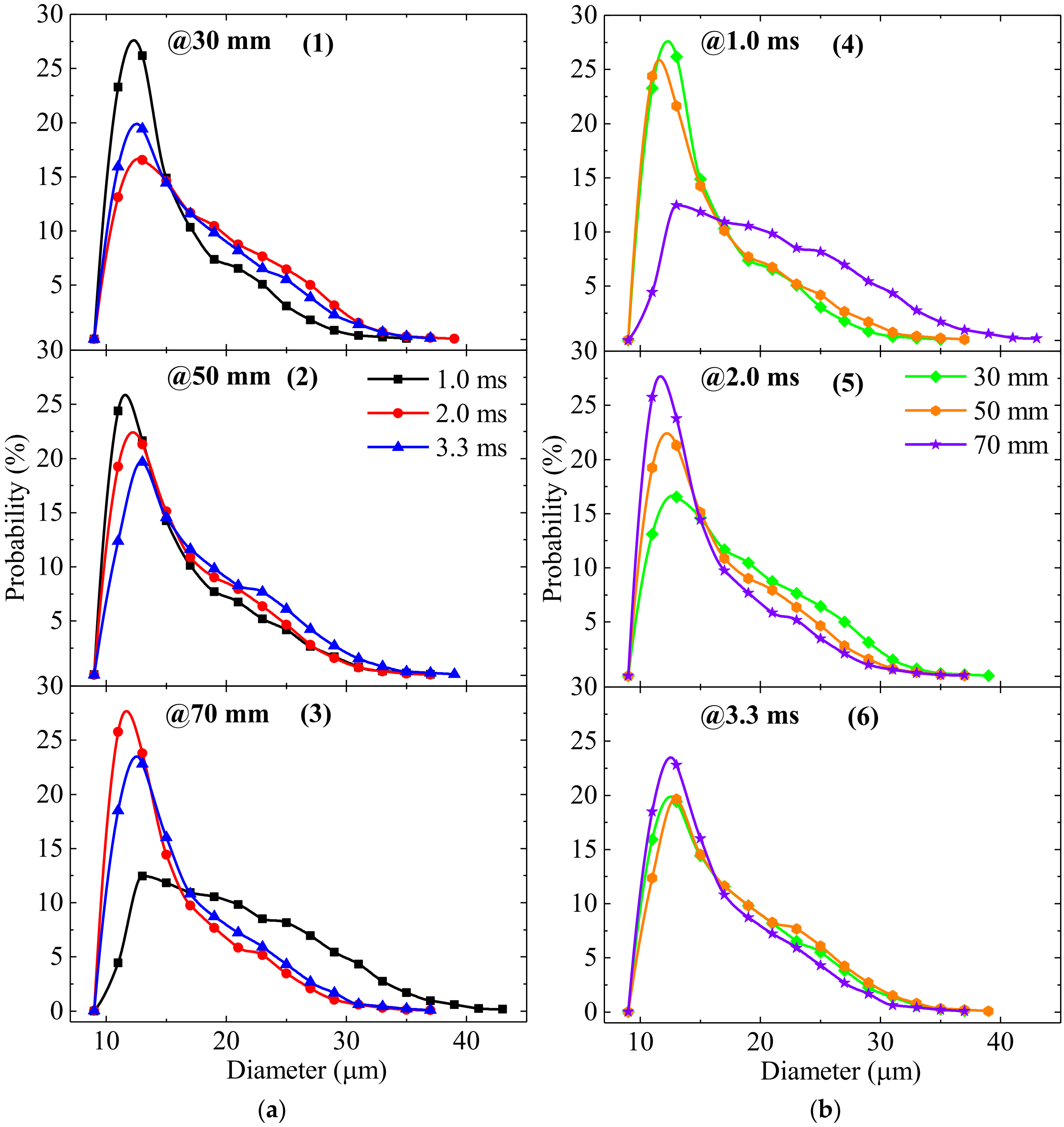

Figure 12. Droplet size. (**a**) Different timings at same location ((1) 30 mm, (2) 50 mm, and (3) 70 mm); (**b**) different locations at same timing ((4) 1.0 ms, (5) 2.0 ms and (6) 3.3 ms).

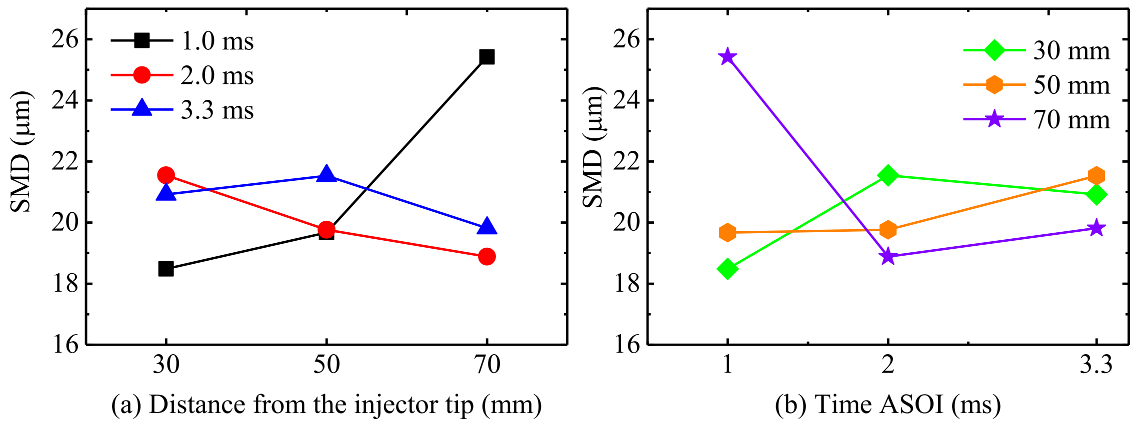

Figure 13. Sauter mean diameter.

3.4. Mean Minimum Distance of Droplets

The mean MD of droplets is shown in Figure 14. The details on defining the MD are provided in Figure 6. The mean MD indicates the degree of the droplet number density at a fixed size window. To investigate the effect of timing on the mean MD, note that the mean MDs at 2.0 and 3.3 ms ASOI considerably exceed that at 1.0 ms, indicating that the droplets disperse better with time. In investigating the effect of location on the mean MD, the mean MD at midstream is found to considerably exceed the mean MDs at upstream and downstream, indicating the good dispersion of droplets at midstream.

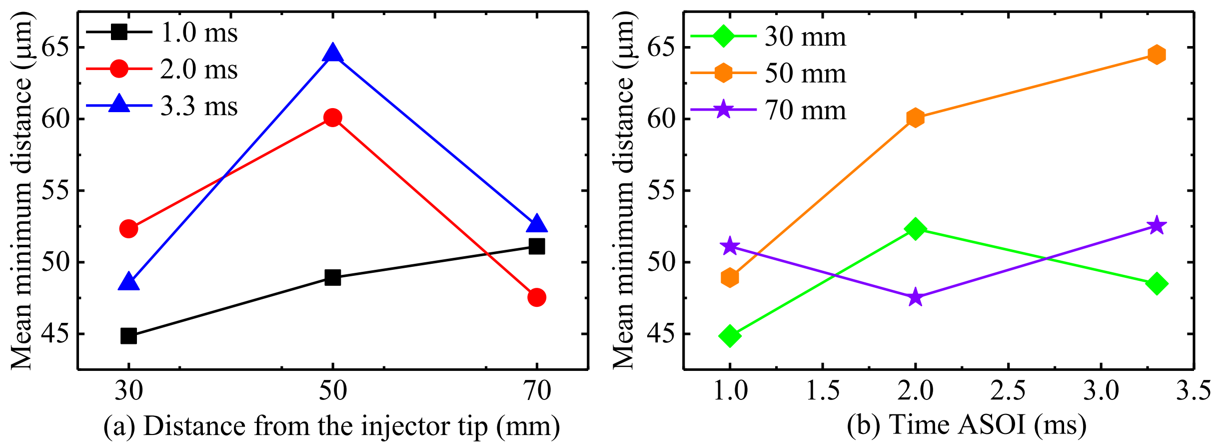

Figure 14. Mean minimum distance.

The velocity–MD distribution with *We* is shown in Figure 15. The horizontal and vertical axes represent the droplet velocity and MD, respectively. The transitions to the deformation regimes are critical because they specify the conditions under which droplets break up. The deformation regimes with increasing *We*, obtained from Hsiang and Faeth [36], are as follows: 5% deformation, We = 0.6; 10% deformation, We = 1.0; 20% deformation, We = 2.1; oscillatory deformation, We = 3.0; and bag breakup, We = 13. The definitions of the deformation and deformation regime details are reported by Hsiang and Faeth (1995). The colored dots in Figure 15 represent the droplets with different We values. When $We \leq 0.6$, $0.6 < We \leq 1.0$, $1.0 < We \leq 2.1$, and $2.1 < We \leq 3.0$; the deformations of droplets are less than 5%, 5–10%, 10–20%, and from 20% to oscillatory deformation, respectively. A change in droplet state from oscillatory deformation to bag breakup indicates that droplets with high *We* can break up. Moreover, in all cases, *We* never exceeds 13. The evident phenomenon is that the number of droplets with a *We* value greater than 0.6 at 1.0 ms exceeds those at 2.0 and 3.3 ms ASOI. At 1.0 ms ASOI, the number of droplets with *We* values exceeding 0.6 increases from upstream to downstream. In particular, the *We* values of most droplets downstream are larger than 0.6. Droplets with larger *We* values have considerable deformation, and those with *We* values exceeding 3 tend to break up into smaller droplets. Moreover, droplets with a high *We* values have small MDs, indicating that they are near the dense spray tip region. A possible reason for the foregoing is that the droplets at 1.0 ms are at the initial stage. Hence, these droplets, particularly those located 70 mm from the spray tip, momentarily have high momentum. However, at 2.0 and 3.3 ms ASOI, from upstream to downstream, the droplet behaviors are similar. The *We* values of most droplets are less than 0.6, and the number of droplets with *We* values exceeding 0.6 decreases from upstream to downstream. Moreover, no droplets with *We* values greater than 1 exist at midstream and downstream. This is because the droplets at 2.0 and 3.3 ms are at the quasi-steady and end stages. Hence, they have lost most of their kinetic energy due to air resistance. Finally, the velocity of droplets is less than 30 m/s at all locations, except for the droplets downstream at 1.0 ms.

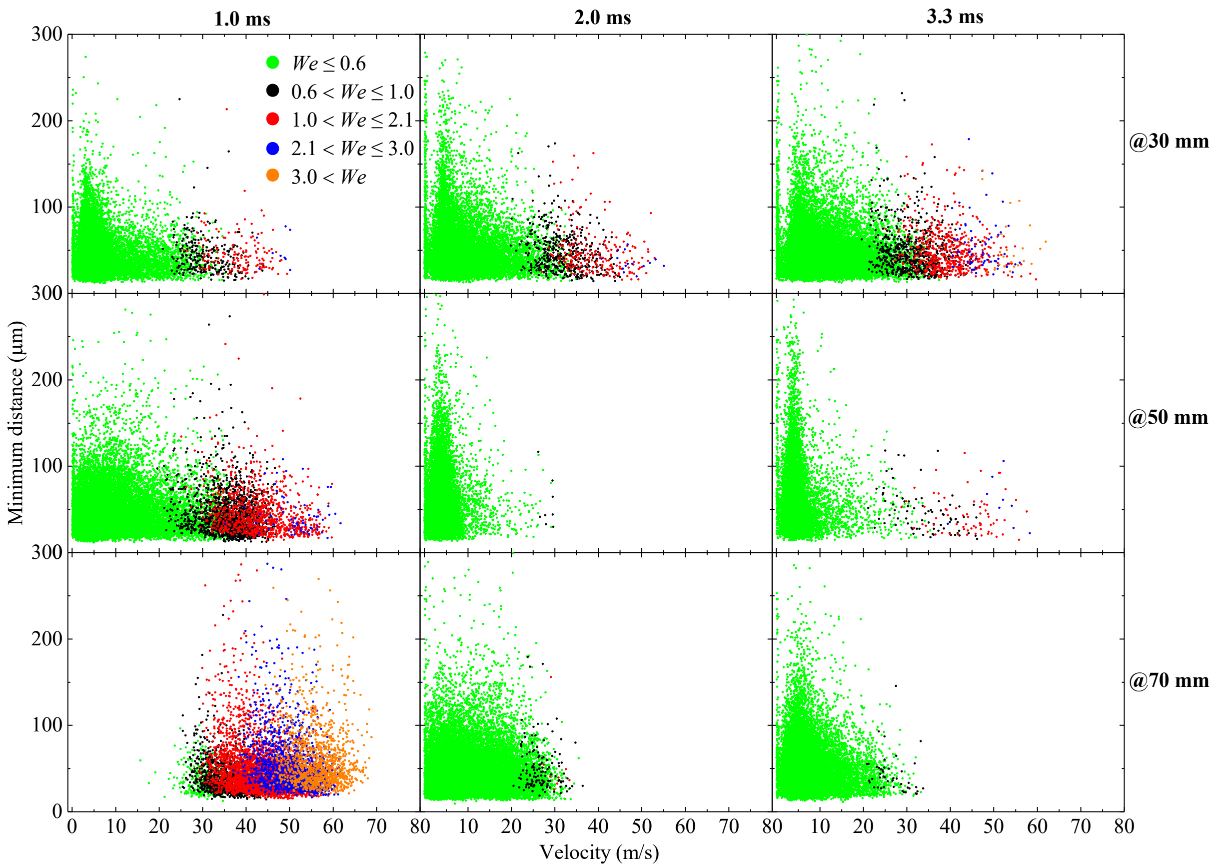

Figure 15. Velocity–MD distribution with *We*.

In summary, the spatial distribution of droplets at the periphery and the three main factors, i.e., mean velocity, mean MD, and SMD, are shown in Figure 16. The tendencies of mean velocity and SMD at 2.0 (Figure 16b) and 3.3 ms (Figure 16c) ASOI are similar from upstream to downstream. However, at 1.0 ms (Figure 16a), the mean velocity and mean MD increase obviously from upstream to downstream. This possibly occurs because the droplets at 1.0 ms are in the initial stage, thus possessing high momentum. This is consistent with the findings of Zhou et al.; they found the average droplet velocity exhibited an obvious acceleration with increasing axial distance [34]. These droplets located at 70 mm are from the spray tip. The mean MD is maximum at midstream, indicating the better dispersion of droplets at this location. As for the application of this work, the geometric parameter of droplets and the key stage selection are significant for evaluating the interaction between the droplets and the surface [37].

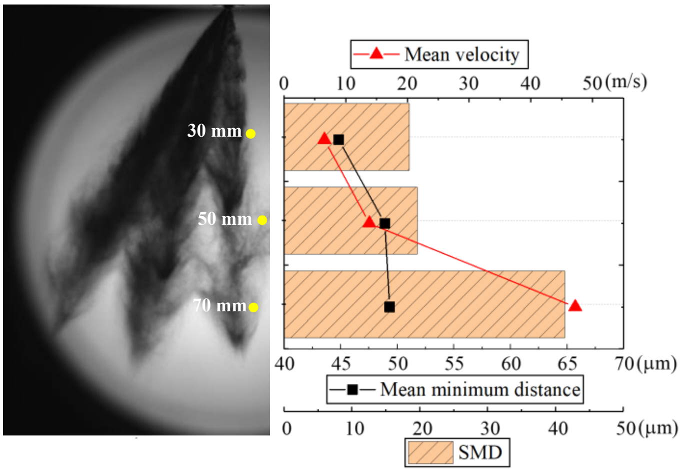

(a) 1.0 ms ASOI (Initial stage)

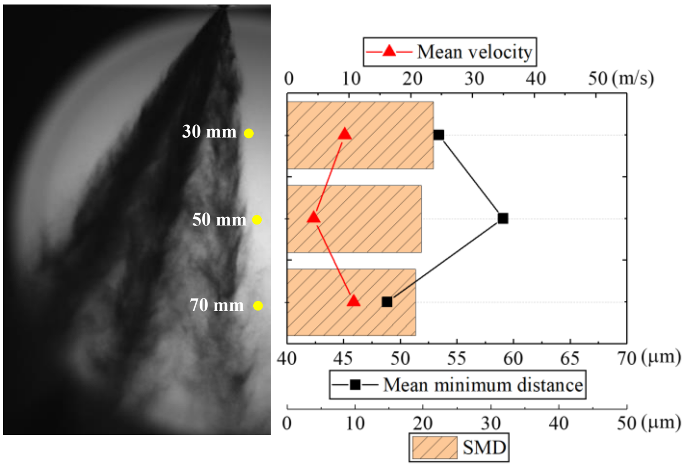

(b) 2.0 ms ASOI (Quasi-steady stage)

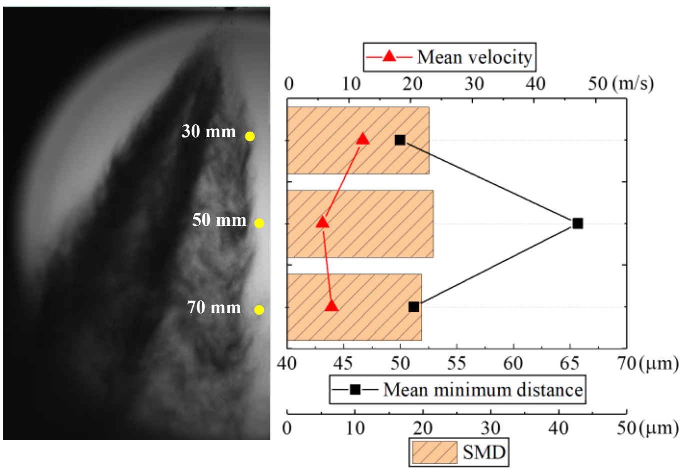

(c) 3.3 ms ASOI (End stage)

Figure 16. Droplet distribution at periphery.

4. Conclusions

An experimental investigation of the microscopic characteristics during the spray breakup process at different stages has been performed. The variations in the droplet behaviors between different stages and locations were also compared. A deeper understanding of droplet behaviors can guide reasonable stage selection, improve thermal efficiency, and ensure accurate application. The main conclusions are as follows:

(1) At the initial stage, the velocity of downstream droplets is much higher than those of the other cases. This is because the capture location was near the spray tip where droplets are larger and have high velocity. The foregoing plays an important role in the axial and radial expansions of the spray at the initial stage. Moreover, the droplet size increases from upstream to downstream. The ligaments easily break up into larger droplets due to aerodynamic resistance. However, at the quasi-steady and end stages, the droplet size and velocity distribution are similar from upstream to downstream.
(2) The mean MDs at the quasi-steady and end stages considerably exceed that at the initial stage, indicating that the droplet dispersion improves with time. However, the mean MD at midstream is much larger than the mean MDs at upstream and downstream. This indicates that the droplets at midstream disperse better than those at upstream and downstream.

Author Contributions: Conceptualization, F.C. and H.L.; methodology, F.C. and H.L.; validation, H.L.; formal analysis, F.C.; investigation, F.C. and H.L.; resources, K.N., R.H., K.U. and W.Z.; data curation, F.C.; writing—original draft preparation, F.C.; writing—review and editing, H.L., P.D., K.N. and Y.O.; visualization, F.C.; supervision, H.L. and K.N. All authors have read and agreed to the published version of the manuscript.

Funding: This study is financially supported by the Foundation of State Key Laboratory of Engines [No. K2022-12].

Institutional Review Board Statement: Not applicable.

Informed Consent Statement: Not applicable.

Data Availability Statement: Not applicable.

Acknowledgments: The authors would like to acknowledge the Mazda Motor Corporation for their support of the equipment apparatus.

Conflicts of Interest: The authors declare no conflict of interest.

Abbreviations

ASOI	After the start of injection
CCD	Charge-coupled device
CVC	Constant volume chamber
d	Nozzle hole diameter
DISI	Direct-injection spark-ignition
L/D	Length to diameter
L2F	Laser-2-focus
MD	Minimum distance
PIA	Particle image analysis
PIV	Particle image velocimetry
PDPA	Phase-Doppler particle analyzer
PDA	Phase-Doppler anemometry
PDIA	Particle/droplet image analysis
P_{inj}	Injection Pressure
P_{amb}	Ambient pressure
SMD	Sauter mean diameter
T_{amb}	Ambient temperature
We	Weber number

References

1. Lee, Z.; Kim, T.; Park, S. Review on spray, combustion, and emission characteristics of recent developed direct-injection spark ignition (DISI) engine system with multi-hole type injector. *Fuel* **2020**, *259*, 116209. [CrossRef]
2. Fansler, T.D.; Parrish, S.E. Spray measurement technology: A review. *Measur. Sci. Technol.* **2015**, *26*, 012002. [CrossRef]

3. Urbán, A.; Zaremba, M.; Malý, M.; Józsa, V.; Jedelský, J. Droplet dynamics and size characterization of high-velocity airblast atomization. *Int. J. Multiph. Flow.* **2017**, *95*, 1–11. [CrossRef]
4. Deshmukh, D.; Ravikrishna, R.V. Studies on microscopic structure of diesel sprays under atmospheric and high gas pressures. *Int. J. Spray Combust. Dyn.* **2014**, *6*, 199–220. [CrossRef]
5. Kashdan, J.T.; Shrimpton, J.S.; Whybrew, A. A digital image analysis technique for quantitative characterisation of high-speed sprays. *Opt. Lasers Eng.* **2007**, *45*, 106–115. [CrossRef]
6. Blaisot, J.; Yon, J. Droplet size and morphology characterization for dense sprays by image processing: Application to the diesel spray. *Exp. Fluids* **2005**, *39*, 977–994. [CrossRef]
7. Komada, K.; Sakaguchi, D.; Tajima, H.; Ueki, H.; Ishida, M. Relation between tip penetration and droplet size of diesel spray. *SAE* **2013**, *2*, 01487191.
8. Goldsworthy, L.; Bong, C.; Brandner, P.A. Measurements of diesel spray dynamics and the influence of fuel viscosity using PIV and shadowgraphy. *Atom. Sprays* **2011**, *21*, 167–178. [CrossRef]
9. Pathania, R.S.; Chakravarthy, S.R.; Mehta, P.S. Time-resolved characterization of low-pressure pulsed injector. *Atom. Sprays* **2016**, *26*, 755–773. [CrossRef]
10. Jing, D.; Zhang, F.; Li, Y.; Xu, H.; Shuai, S. Experimental investigation on the macroscopic and microscopic spray characteristics of dieseline fuel. *Fuel* **2017**, *199*, 478–487. [CrossRef]
11. Wang, Z.; Xu, H.; Jiang, C.; Wyszynski, M.L. Experimental study on microscopic and macroscopic characteristics of diesel spray with split injection. *Fuel* **2016**, *174*, 140–152. [CrossRef]
12. Krzeczkowski, S.A. Measurement of liquid droplet disintegration mechanism. *Int. J. Multiphase Flow* **1980**, *6*, 227–239. [CrossRef]
13. Dai, Z.; Faeth, G.M. Temporal properties of secondary drop breakup in the multimode breakup regime. *Int. J. Multiphase Flow* **2001**, *27*, 217–236. [CrossRef]
14. Feng, Z.; Tang, C.; Yin, Y.; Zhang, P.; Huang, Z. Time-resolved droplet size and velocity distributions in a dilute region of a high-pressure pulsed diesel spray. *Int. J. Heat. Mass Transfer.* **2019**, *133*, 745–755. [CrossRef]
15. Lebedevas, S.; Klyus, O.; Raslavičius, L.; Krause, P.; Rapalis, P. Findings on droplet breakup behavior of the preheated microalgae oil jet for efficiency improvement in diesel engines. *Biomass Conv. Bioref.* **2022**, *21*, 2162. [CrossRef]
16. Luo, H.; Nishida, K.; Ogata, Y.; Zhang, W. Microscopic characteristics of near-nozzle spray at the initial and end stages. *Fuel* **2021**, *283*, 118953. [CrossRef]
17. Bae, C.; Kang, J. The structure of a break-up zone in the transient diesel spray of a valve-covered orifice nozzle. *Int. J. Engine Res.* **2006**, *7*, 319–334. [CrossRef]
18. Payri, R.; Tormos, B.; Salvador, F.J.; Araneo, L. Spray droplet velocity characterization for convergent nozzles with three different diameters. *Fuel* **2008**, *87*, 3176–3182. [CrossRef]
19. Liu, M.; Duan, Y.F.; Zhang, T.N. Evaluation of effervescent atomizer internal design on the spray unsteadiness using a phase/doppler particle analyzer. *Exp. Therm. Fluid Sci.* **2010**, *34*, 657–665. [CrossRef]
20. Crua, C.; Shoba, T.; Heikal, M.; Gold, M.; Higham, C. High-speed microscopic imaging of the initial stage of diesel spray formation and primary breakup. *SAE Paper* **2010**, *1*, 2247.
21. Pei, Y.; Qin, J.; Li, X.; Zhang, D.; Wang, K.; Liu, Y. Experimental investigation on free and impingement spray fueled with methanol, ethanol, isooctane, TRF and gasoline. *Fuel* **2017**, *208*, 174–183. [CrossRef]
22. Wang, Z.; Hopfes, T.; Giglmaier, M.; Adams, N.A. Experimental investigation of shock-induced tandem droplet breakup. *Phys. Fluids* **2021**, *33*, 012113. [CrossRef]
23. Zhao, H.; Wu, Z.; Li, W.; Xu, J.; Liu, H. Interaction of two drops in the bag breakup regime by a continuous air jet. *Fuel* **2019**, *236*, 843–850. [CrossRef]
24. Chen, Y.; Liu, S.; Guo, X.; Jia, C.; Huang, X.; Wang, Y.; Huang, H. Experimental research on the macroscopic and microscopic spray characteristics of diesel-$PODE_{3–4}$ blends. *Energies* **2021**, *14*, 5559. [CrossRef]
25. Khaleghi, H.; Farani Sani, H.; Ahmadi, M.; Mohammadzadeh, F. Effects of turbulence on the secondary breakup of droplets in diesel fuel sprays. *Proc. Inst. Mechan. Eng. Part D J. Automob. Eng.* **2021**, *235*, 387–399. [CrossRef]
26. Amedorme, S. Experimental study of mean droplet size from pressure swirl atomizer. *Int. J. Eng. Sci. Technol.* **2020**, *4*, 49–59. [CrossRef]
27. Chang, F.; Luo, H.; Zhan, C.; Nishida, K.; Ogata, Y. Droplets velocity and diameter variations of wall impinging spray created by slicer. *Fuel* **2021**, *299*, 120894. [CrossRef]
28. Luo, H.; Ogata, Y.; Nishida, K. Effects of droplet behaviors on fuel adhesion of flat wall impinging spray injected by a DISI injector. *SAE Tech. Pap.* **2019**, *24*, 34.
29. Zhan, C.; Luo, H.; Chang, F.; Nishida, K.; Ogata, Y.; Tang, C.; Feng, Z.; Huang, Z. Experimental study on the droplet characteristics in the spray tip region: Comparison between the free and impinging spray. *Exp. Therm. Fluid Sci.* **2021**, *121*, 894–1777. [CrossRef]
30. Postrioti, L.; Buitoni, G.; Pesce, F.; Ciaravino, C. Zeuch method-based injection rate analysis of a common rail system operated with advanced injection strategies. *Fuel* **2014**, *128*, 188–198. [CrossRef]
31. Wang, C.; Wang, Y.; Zhu, J.; Long, W.; Nishida, K. Design and application of an algorithm for measuring particle velocity based on multiple characteristics of a particle. *Fuel* **2020**, *271*, 117605. [CrossRef]
32. Luo, H.; Wang, C.; Nishida, K.; Ogata, Y.; Chen, R. Characteristics of droplet behaviors after the end of injection in a high-pressure constant volume chamber. *Fuel* **2020**, *267*, 117291. [CrossRef]

33. Qian, J.; Law, C.K. Regimes of coalescence and separation in droplet collision. *J. Fluid Mech.* **1997**, *331*, 59–80. [CrossRef]
34. Zhou, Z.F.; Yin, J.; Yang, X.Y.; Chen, B.; Liu, B. Experimental investigation on the macroscopic spray and microscopic droplet diameter, velocity and temperature of R404A flashing spray. *Int. J. Heat Mass Transf.* **2021**, *177*, 121546. [CrossRef]
35. Lee, S.; Oh, Y.; Park, S. Characterization of the spray atomization process of a multi-hole gasoline direct injector based on measurements using a phase Doppler particle analyser. *Proc. Inst. Mech. Eng. Part D J Automob. Eng.* **2013**, *227*, 951–965. [CrossRef]
36. Faeth, G.M.; Hsiang, L.P.; Wu, P.K. Structure and breakup properties of sprays. *Int. J. Multiphase Flow* **1995**, *21*, 99–127. [CrossRef]
37. Wang, X.L.; Qu, Z.G.; Lai, T.; Ren, G.F.; Wang, W.K. Enhancing water transport performance of gas diffusion layers through coupling manipulation of pore structure and hydrophobicity. *J. Power Sources* **2022**, *525*, 231121. [CrossRef]